

Article

Co-Design Optimization and Total Cost of Ownership Analysis of an Electric Bus Depot Microgrid with Photovoltaics and Energy Storage Systems

Boud Verbrugge ^{1,2} , Thomas Geury ^{1,2}  and Omar Hegazy ^{1,2,*} 

¹ MOBI-EPOWERS Research Group, ETEC Department, Vrije Universiteit Brussel (VUB), Pleinlaan 2, 1050 Brussel, Belgium; boud.verbrugge@vub.be (B.V.); thomas.geury@vub.be (T.G.)

² Flanders Make, Gaston Geenslaan 8, 3001 Heverlee, Belgium

* Correspondence: omar.hegazy@vub.be

Abstract: Due to the increasing share of battery electric buses (BEBs) in cities, depots need to be adapted to the increasing load demand. The integration of renewable energy sources (RESs) into a depot can increase the self-consumption, but optimal sizing is required for a cost-efficient and reliable operation. Accordingly, this paper introduces a co-design optimization framework for a depot microgrid, equipped with photovoltaics (PVs) and an energy storage system (ESS). Three European cities are considered to evaluate the effect of different environmental conditions and electricity prices on the optimal microgrid design. Accurate models of the different subsystems are created to estimate the load demand and the power generation. Different energy management strategies (EMSs), developed to properly control the power flow within the microgrid, are compared in terms of operational costs reduction, one of which was also experimentally validated using a hardware-in-the-loop (HiL) test setup. In addition, the total cost of ownership (TCO) of the depot microgrid is analyzed, showing that an optimally designed depot microgrid can reduce the charging-related expenses for the public transport operator (PTO) by 30% compared to a scenario in which only the distribution grid supplies the BEB depot.

Keywords: electric buses; depot charging; DC microgrid; co-design optimization; energy management; TCO analysis; hardware-in-the-loop testing



Citation: Verbrugge, B.; Geury, T.; Hegazy, O. Co-Design Optimization and Total Cost of Ownership Analysis of an Electric Bus Depot Microgrid with Photovoltaics and Energy Storage Systems. *Energies* **2024**, *17*, 6233. <https://doi.org/10.3390/en17246233>

Academic Editor: Rui Xiong

Received: 24 October 2024

Revised: 2 December 2024

Accepted: 5 December 2024

Published: 11 December 2024



Copyright: © 2024 by the authors. Licensee MDPI, Basel, Switzerland. This article is an open access article distributed under the terms and conditions of the Creative Commons Attribution (CC BY) license (<https://creativecommons.org/licenses/by/4.0/>).

1. Introduction

Public transport operators (PTOs) in European cities are striving for zero-emission transportation, which has resulted in a sharp increase in sales of battery electric buses (BEBs) in the last years [1]. However, as these BEBs typically require high charging power (>100 kW), it is clear that the distribution grid will not be able to deal with these additional loads without being reinforced at bus depots, which are one of the main locations for charging BEBs. However, such a grid reinforcement is expensive for PTOs and has no effect on the electricity costs associated with BEB charging. Accordingly, other approaches are required to reshape BEB depots and enable a smooth transition to fully electrified transportation.

One interesting idea is to integrate a BEB depot in a microgrid, a well-established concept within the scientific literature, to increase the depot's self-sufficiency. A microgrid is a flexible entity where local renewable energy sources (RESs), like photovoltaics (PVs), energy storage systems (ESSs), and controllable loads are incorporated with the intention to operate more autonomously from the main distribution grid [2]. An energy management strategy (EMS) is essential to maintain the energy balance between the subsystems and to realize an economic, efficient, and reliable operation [3]. Different microgrid topologies (AC, DC, and hybrid) can be distinguished depending on the type of voltage that links the various elements.

The possible benefits of merging a BEB depot into a microgrid have been addressed in recent studies. Dougier et al. [4] highlighted that an ESS increases the benefits from PV systems for charging BEBs during the summer. In [5], the authors investigated the techno-economic feasibility of a hybrid grid-connected PV system for a BEB depot and found that it could reduce the total costs by 4% compared with a grid-only depot configuration. Arif et al. [6] proposed an EMS for a microgrid depot to maximize the daily profit of the PTO. Depending on the season, they managed to increase the profit by 11–68% compared with a depot without an integrated microgrid. Zhuang et al. [7] presented a stochastic EMS using dynamic prices to minimize the charging cost and mitigate the charging impact on the distribution network, which actually increased the cost by 9%. A similar study was performed by Liu et al. [8]. They proposed a three-layer stochastic EMS for a BEB transit center with PV infrastructure and ESS to minimize the operational costs and optimize the local voltage quality. With their EMS, they achieved a cost reduction of 12% compared with other EMSs. In [9], the authors developed a bi-level optimal scheduling framework to incorporate BEBs with vehicle-to-grid (V2G) capabilities into a regional integrated energy system. Their strategies could effectively reduce the total operational costs by up to 40% compared with uncoordinated charging. Ren et al. [10] proposed an optimal deployment strategy of distributed rooftop PV systems and ESSs from a neighboring community to supply BEBs, which resulted in a payback period of 4 years.

While the aforementioned studies obtained meaningful results, there is still room for improvement. Generally, a total cost of ownership (TCO) analysis was not executed, which is an important factor for PTOs. Despite an optimal EMS that can significantly reduce the operation cost, the high investment cost of oversized microgrid sub-systems could potentially cancel out the lower operational costs and lead to a higher TCO. Optimal sizing of the subsystems is indispensable when establishing a depot microgrid [11]. Furthermore, mainly an AC microgrid was considered in the precedent studies. However, for a BEB depot, a DC microgrid is the preferred option because it facilitates the integration of RESs, ESSs, and the charging infrastructure. DC microgrids also have the advantage that they are easier to control due to the absence of frequency regulation and reactive power flow management. They are also more efficient, more reliable, and have lower operating costs than their AC counterparts [12,13]. Finally, these studies only verified their EMS algorithms through offline simulation models. Although model-based simulations offer valuable insights into how the charging process of BEBs can be enhanced, they cannot predict whether these EMS techniques will work as intended with real hardware. Experimental validation is required to verify the performance of the established EMS in real-world conditions. To avoid time-consuming tests, reduce the costs associated with it, accelerate the development of an EMS, and facilitate its integration, hardware-in-the-loop (HiL) tests can be executed [14,15]. HiL testing is a method that enables a high-fidelity experimental validation of control strategies by implementing them in a digital real-time simulation platform that interacts with a realistic environment. Recently, HiL testing has sporadically been used for microgrid applications. Mahmud et al. [16] performed a grid impact analysis of high-power charging infrastructure with integrated PV system and ESS using HiL experiments. Also, in [17–19], advanced test platforms to verify EMS algorithms for microgrids in real-time were presented.

This paper addresses these shortcomings by presenting a co-design optimization framework, which integrates and combines an EMS and sizing algorithm, to optimally design and control a DC microgrid for BEB depots and aims to minimize the TCO for the PTO. In addition, a TCO comparison with other depot configurations is executed to analyze the cost benefits of such a depot microgrid and the developed EMS is experimentally validated using an HiL setup of a DC microgrid existing of real components and emulators to demonstrate its operation in a relevant environment. Accordingly, this paper provides a complete overview for PTOs on the operation and benefits of a depot microgrid.

The remainder of this paper is organized as follows. In Section 2, the co-design optimization framework to obtain the optimal size of the components and EMS parameters is

described. This section also includes the accurate modelling of the microgrid's subsystems to have a precise estimation of the consumed power within the microgrid and the development of the EMS. Section 3 presents the simulation results of some pre-defined use cases to verify the applicability of a depot microgrid and its EMS, together with a detailed TCO comparison of the depot microgrid and the experimental validation of the EMS on an HiL test setup. Finally, the conclusions are formulated in Section 4.

2. Methodology

2.1. Microgrid Architecture and Modelling

The considered depot microgrid comprises a PV array and an ESS in addition to the charging infrastructure of the BEBs and the connection to the distribution grid. These elements are each connected to a common DC link through interfacing power electronics converters (PECs). A complete overview of the depot microgrid architecture is depicted in Figure 1. During the day, BEBs can be charged with solar power coming from the PV infrastructure. As such, less power is required from the distribution grid, which reduces the electricity costs for the PTO. The ESS is employed to compensate the intermittency of the PV infrastructure and balance the inevitable mismatch between the charging load of the BEBs and the locally produced power. In Figure 1, the ESS is illustrated as a stationary battery pack, but spare BEBs, which are not in operation during the day, could theoretically be used as well.

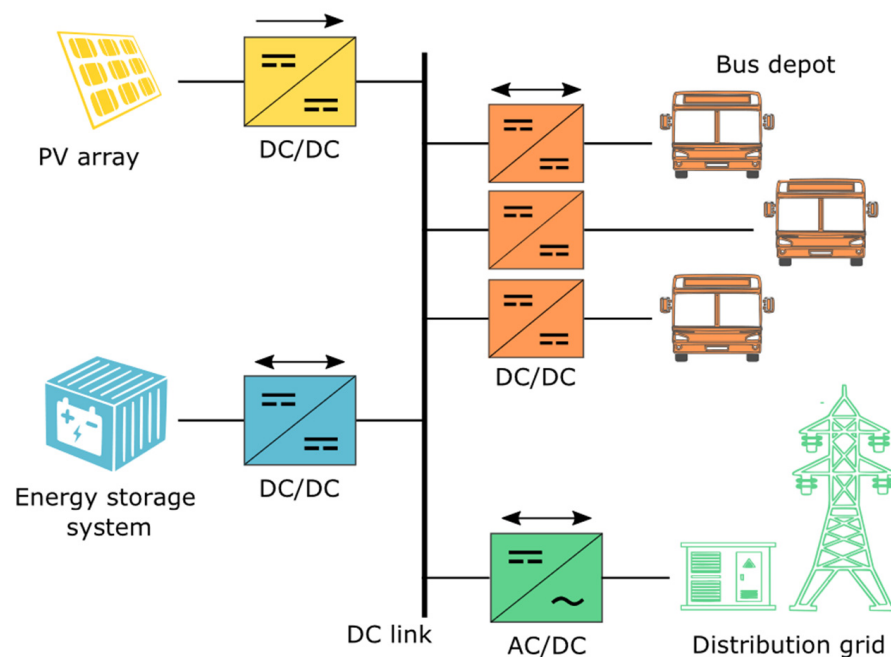


Figure 1. Overview of the architecture of the depot microgrid.

2.1.1. Depot Charging Infrastructure

The charging infrastructure in the depot consists of multiple DC charging points, to which a BEB can be connected, and (modular) bidirectional DC/DC converters in between the DC link and the charging points. Each charging point receives a current signal based on the optimal charging schedule provided by a high-level charging management system (HL-CMS), as described in [20].

The bidirectional DC/DC converters are modelled using a look-up table (LuT), specifying the efficiency at different voltage and current levels. The efficiency map is derived from a high-fidelity loss model of a SiC-based DC/DC converter, which is used to calculate

the load current $I_{load,(dis)charging}$ of each charging point based on the requested charging or discharging current, as stated in Equations (1) and (2).

$$I_{load,charging} = \frac{V_{BEB} \cdot I_{charging}}{\eta_{DC/DC,load} \cdot V_{DClink}} \tag{1}$$

$$I_{load,discharging} = \frac{\eta_{DC/DC,load}^* \cdot V_{BEB} \cdot I_{discharging}}{V_{DClink}} \tag{2}$$

where $\eta_{DC/DC,load}$ is the efficiency of the DC/DC converter at a specific voltage V_{BEB} and current $I_{charging}$ during charging, $\eta_{DC/DC,load}^*$ is the efficiency of the same converter during discharging, and V_{DClink} is the voltage of the DC link.

The total current $I_{depot,tot}$ that is required to charge or discharge the BEBs in the depot can be computed by adding up the currents of each charging point as expressed in Equation (3).

$$I_{depot,tot} = \sum_i I_{load,(dis)charging_i} \tag{3}$$

2.1.2. PV Infrastructure

The PV infrastructure consists of a PV array and a DC/DC converter. The PV array is composed of multiple PV modules to attain the required voltage and current output. However, the output power of the PV array highly depends on the actual environmental conditions such as the irradiance and the temperature. The DC/DC converter is required to maximize the output power of the PV array. A maximum power point tracking (MPPT) technique allows the PV array to be constantly operated at maximum power by changing the duty ratio of the converter. Many different techniques exist to determine the maximum power point [21,22]. However, they do not need to be explicitly implemented to model the PV infrastructure. To represent the PV modules, the single-diode model is used. It consists of a current source connected with an anti-parallel diode, a shunt resistance R_{sh} and a series resistance R_s , as shown in Figure 2.

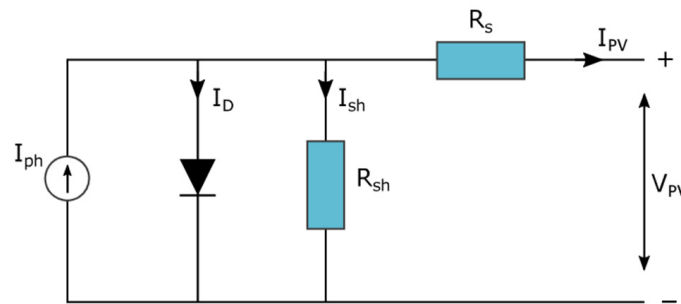


Figure 2. Single-diode model of a PV module.

By utilizing Kirchhoff’s current law, the current I_{PV} generated by the PV module can be calculated, as expressed in Equation (4).

$$I_{PV} = I_{ph} - I_D - I_{sh} = I_{ph} - I_D - \frac{V_{PV} + R_s \cdot I_{PV}}{R_{sh}} \tag{4}$$

where I_{ph} is the photo-generated current [A], I_D is the current flowing through the diode [A], I_{sh} is the leakage current in the shunt resistance [A], and V_{PV} is the terminal voltage of the PV module [V].

The diode current is proportional with the reverse saturation current according to the Shockley diode law, as expressed in Equation (5).

$$I_D = I_{sat} \cdot \left[e^{\left(\frac{q \cdot (V_{PV} + R_s \cdot I_{PV})}{k \cdot Q_d \cdot T_c \cdot N_c} \right)} - 1 \right] \tag{5}$$

where N_c is the number of PV cells in series that assemble the PV module, T_c is the cell operating temperature [K], Q_d is the diode ideality factor, $q = 1.60 \times 10^{-19}$ is the electron charge [C], and $k = 1.38 \times 10^{-23}$ is the Boltzmann constant [J/K].

To effectively model the PV infrastructure, five parameters (I_{ph} , I_{sat} , R_s , R_{sh} , and Q_d) must be determined. They are estimated from the manufacturer’s datasheet using the analytical method described in [23], by taking into account the effect of the varying irradiance and temperature on their behavior.

As the PV array consists of multiple PV modules connected in series and in parallel to attain a certain voltage and current level, I_{ph} and I_{sat} should be multiplied with the number of modules connected in parallel $N_{p,PV}$, while V_{PV} should be multiplied with the number of modules connected in series $N_{s,PV}$. Finally, both the series and shunt resistances must be increased with the ratio $N_{s,PV}/N_{p,PV}$, respectively.

The total current of the PV array at the maximum power point $I_{PV,mpp,tot}$ is calculated by solving Equation (4) at its maximum power point voltage $V_{PV,mpp,tot}$, considering the updated values of the aforementioned parameters.

The DC/DC converter is modelled as an LuT representing its efficiency. The current at the output of the converter $I_{PV,out,tot}$ can be determined as stated in Equation (6).

$$I_{PV,out,tot} = \frac{\eta_{DC/DC,PV} \cdot V_{PV,mpp,tot} \cdot I_{PV,mpp,tot}}{V_{DClink}} \tag{6}$$

2.1.3. Energy Storage System

The ESS contains multiple battery cells, divided into different modules, that are connected with each other in series and parallel. A single battery cell is modelled using the first-order Thevenin model. Its equivalent circuit diagram is presented in Figure 3. It connects an ideal voltage source with a resistance and a parallel RC network that accounts for the polarization effects.

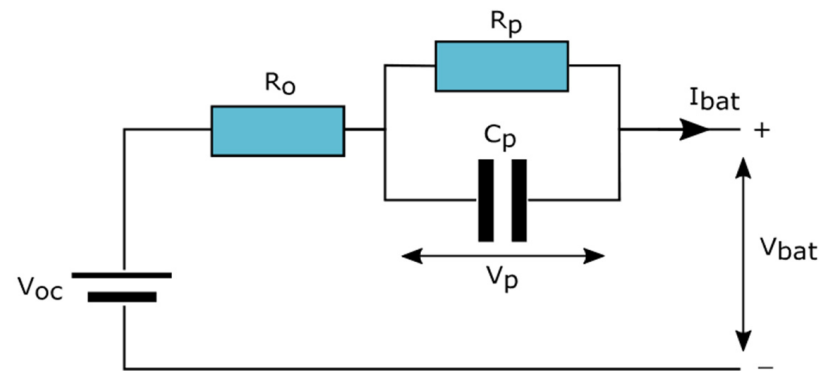


Figure 3. Equivalent circuit diagram of a first-order Thevenin model.

The electrical behavior of the model is described in Equation (7) and allows to compute the terminal battery cell voltage V_{bat} based on the current I_{bat} that flows through it. I_{bat} equals the current that needs to be provided by or stored in the ESS, $I_{ESS,tot}$, divided by the number of parallel battery strings $N_{p,bat}$.

$$\begin{cases} \dot{V}_p = -\frac{V_p}{R_p \cdot C_p} + \frac{I_{bat}}{C_p} \\ V_{bat} = V_{oc} - V_p - R_o \cdot I_{bat} \end{cases} \tag{7}$$

where V_{oc} denotes the open-circuit voltage (OCV) [V] and V_p the polarization voltage over the RC network [V]. R_o and R_p are the ohmic resistance and the polarization resis-

tance, respectively, and represent the internal battery resistance [Ω]. C_p is the polarization capacitance and characterizes the transient response of the battery [F].

The OCV depends on the state-of-charge (SoC) and the battery temperature, while the resistances R_o and R_p and the capacitance C_p are a function of the SoC, the temperature, and the current. The SoC is estimated from the current I_{bat} using the Coulomb counting method. LuTs, generated from experimental data, are used to describe the relationships between these parameters.

The ESS is connected to the DC link with a bidirectional DC/DC converter, modelled as an efficiency map. The current after the converter can be calculated as expressed in Equation (8) when the ESS is discharging and in Equation (9) when the ESS is charging.

$$I_{ESS,out,tot} = \frac{\eta_{DC/DC,ESS} \cdot V_{ESS} \cdot I_{ESS,tot,discharging}}{V_{DClink}} \quad (8)$$

$$I_{ESS,out,tot} = \frac{V_{ESS} \cdot I_{ESS,tot,charging}}{\eta_{DC/DC,ESS}^* \cdot V_{DClink}} \quad (9)$$

where V_{ESS} is the terminal voltage of the ESS [V], which is computed by multiplying V_{bat} with the number of batteries connected in series $N_{s,bat}$.

2.1.4. Distribution Grid

The connection between the DC link and the distribution grid is realized by a two-stage inverter. In the first stage, the incoming AC power of the distribution grid is converted to a fixed DC voltage. The second stage comprises a DC/DC converter to match the voltage of the DC link. Both conversion stages are modelled as LuT efficiency maps. The current at the DC link side $I_{grid,out,tot}$ can be determined as expressed in Equation (10) when the distribution grid provides power to the depot microgrid and in Equation (11) when it is the other way around.

$$I_{grid,out,tot} = \frac{\eta_{DC/DC,grid} \cdot \eta_{AC/DC,grid} \cdot \sqrt{3} \cdot V_{grid} \cdot I_{grid,in,tot} \cdot \cos(\phi)}{V_{DClink}} \quad (10)$$

$$I_{grid,out,tot} = \frac{\sqrt{3} \cdot V_{grid} \cdot I_{grid,in,tot} \cdot \cos(\phi)}{\eta_{DC/DC,grid}^* \cdot \eta_{AC/DC,grid}^* \cdot V_{DClink}} \quad (11)$$

where $I_{grid,in,tot}$ and V_{grid} are the current and the voltage of the distribution grid at the AC side of the inverter and $\cos(\phi)$ is the power factor which is also represented by an LuT.

2.2. Energy Management Strategy

The control of a DC microgrid is a complex task, but it is essential to achieve a stable, reliable, and efficient operation. A hierarchical control structure is frequently adopted because it combines multiple control levels that can operate somewhat independently of one another in different time scales. Hierarchical control generally consists of three levels: primary, secondary, and tertiary control. Primary control regulates the current and voltage output of the PECs in the microgrid with inner loop control and also assures adequate current sharing among the parallel-connected modules with droop control. However, accurate current sharing results in large deviations of the nominal DC link voltage. Therefore, secondary control is responsible for restoring the DC link voltage and improving the power quality by setting a reference for the primary control. Finally, the tertiary and highest control level deals with the energy management of the entire microgrid and focuses mainly on economic dispatch [24–26].

Since this research is focused on reducing the operational costs for the PTO, only the development of an EMS is considered, where it is assumed that the primary and secondary control levels are correctly implemented to ensure a constant DC link voltage and proper current sharing during operation.

An EMS is necessary to continuously control the power flow and guarantee the energy balance within the microgrid depot. Since the current required to charge the BEBs, $I_{\text{depot,out,tot}}$, is fixed by the HL-CMS and the current generated by the PV infrastructure, $I_{\text{PV,out,tot}}$, is controlled by the MPPT technique, the EMS will only need to adjust the current setpoint of the ESS. The current that the distribution grid should give or take can be derived directly from the energy balance equation on the DC link as expressed in Equation (12).

$$I_{\text{depot,out,tot}} - I_{\text{PV,out,tot}} - I_{\text{ESS,out,tot}} - I_{\text{grid,out,tot}} = 0 \quad (12)$$

Two rule-based strategies are proposed, a simple EMS which only considers the imbalance between the current generated by the PV infrastructure and the charging current required for the BEBs, and a more advanced EMS which also considers the actual and future wholesale electricity prices. An overview of the control inputs and output of both methods is depicted in Figure 4, where the tariff is only used for the advanced EMS.

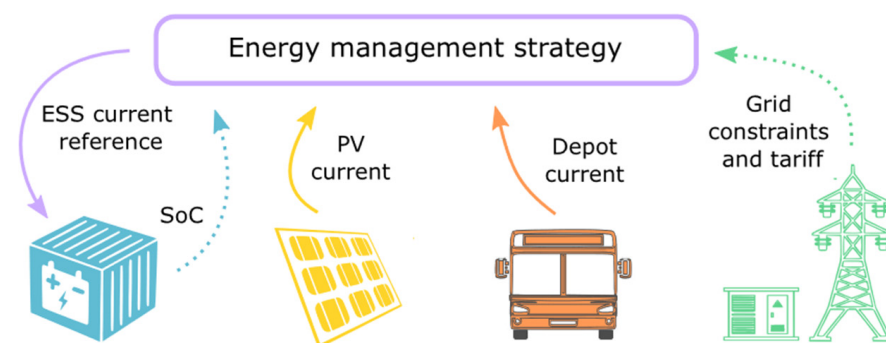


Figure 4. Overview of the control signals of the simple EMS (all, except tariff) and the advanced EMS (all).

2.2.1. Simple EMS

In the simplest EMS, the initial current setpoint of the ESS is always computed as expressed in Equation (13). If the current generated by the PV array is bigger than the current that is needed to charge the BEBs, the ESS will absorb the excess current. Otherwise, the ESS will provide the necessary current to compensate the power imbalance.

$$I_{\text{ESS,out,tot}} = I_{\text{depot,out,tot}} - I_{\text{PV,out,tot}} \quad (13)$$

Since high charging and discharging currents (more than 1C) have an adverse effect on the lifetime of an ESS, a current limit is needed to avoid a fast deterioration. Accordingly, in case such high currents are requested, the initial setpoint will be adjusted and limited to the maximum current with which the ESS can be charged or discharged as expressed in Equation (14).

$$I_{\text{ESS,out,max}} = C_{r,\text{ESS,max}} \cdot E_{\text{bat}} \cdot N_{p,\text{bat}} \quad (14)$$

where $C_{r,\text{ESS,max}}$ denotes the maximum C-rate of the ESS and E_{bat} the rated energy of one battery cell. The maximum C-rate is a variable parameter that needs to be optimized in the co-design optimization framework since it affects the operation of the microgrid.

In case the SoC of the ESS has reached its lower or upper threshold, $I_{\text{ESS,out,tot}}$ will be fixed to zero to extend the lifetime of the ESS. A third constraint that cannot be violated is the grid limitation imposed by the distribution system operator (DSO).

2.2.2. Advanced EMS

The more advanced EMS aims to minimize the electricity cost for the PTO by playing with the dynamic tariff. Therefore, it applies a set of rules which allows the depot microgrid to operate in a variety of situations. Depending on the current coming from the PV array, the current flowing to the depot, the actual electricity price, and the tariff forecasts, the

rules depicted in Figure 5 determine whether the ESS should be charged (highlighted in blue), discharged (green), or not be used (orange).

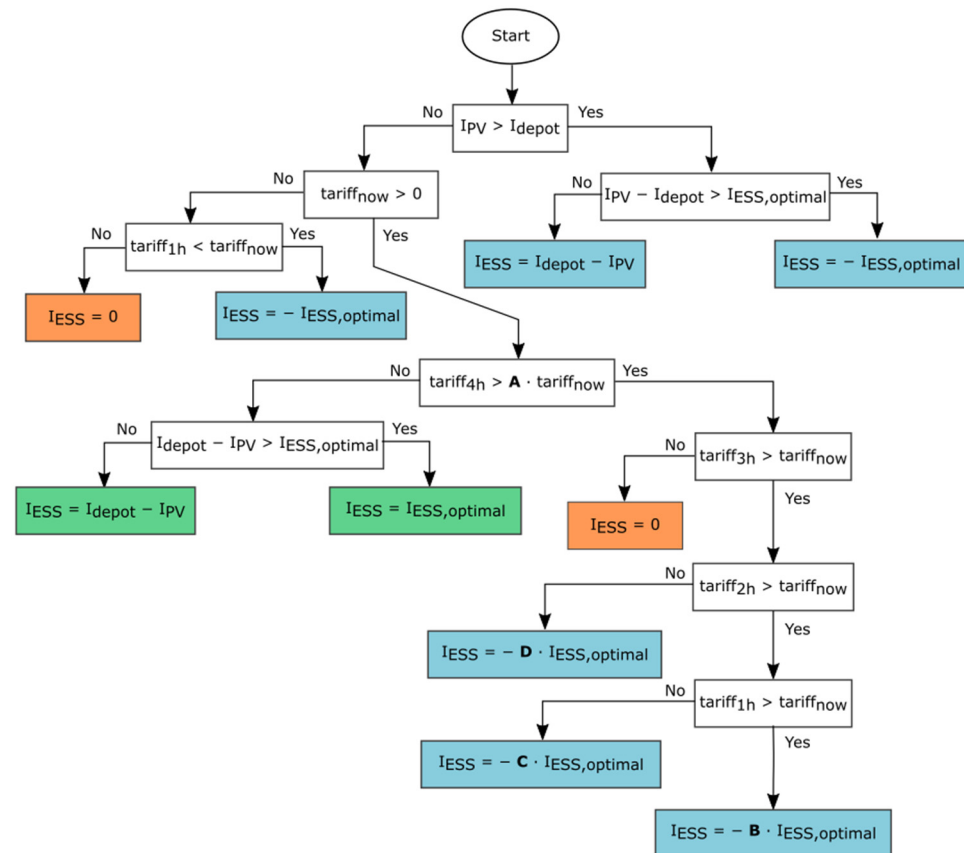


Figure 5. Flowchart of the advanced rule-based EMS.

Compared to the simple EMS, there are four additional design variables (A, B, C, and D in Figure 5), next to the optimal charging and discharging rate, that require optimization. A signifies the minimal difference in electricity price between the current tariff and the forecast of the tariff within 4 h that is required to take advantage of charging the ESS with current from the distribution grid and utilizing it later to charge the BEBs. B, C, and D are constants that specify the amount of current that should be drawn from the grid in function of the optimal current rate.

When the current setpoint for the ESS is determined by the set of rules, it is again checked if the operational constraints of the depot microgrid are not violated. In doing so, the initial setpoint will be adjusted depending on the current limit of the ESS, the SoC level, or the grid limitation.

2.3. Design Optimization

To determine the optimal size of the subsystems of the depot microgrid (PV array, ESS, PECs, and transformer) and the optimal value(s) of the design variable(s) of the EMS, which themselves influence the size of the subsystems, a co-design optimization framework is developed, aiming to minimize the TCO of the depot microgrid over its entire lifetime. A particle swarm optimization (PSO) algorithm is used to solve the co-design optimization problem. PSO is a population-based nature-inspired metaheuristic technique, which can return a good solution within an acceptable convergence time. It is simple to implement and efficient in maintaining the harmony between exploring and exploiting the search space [27]. Accordingly, PSO has already been extensively used for microgrid sizing purposes [28–30].

The PSO algorithm will need to optimize three variables ($N_{p,PV}$, $N_{p,bat}$, and $C_{r,ESS,max}$) in the case of the simple EMS and seven variables ($N_{p,PV}$, $N_{p,bat}$, $C_{r,ESS,max}$, A , B , C , and D) in case of the more advanced EMS. The numbers of parallel PV modules and battery strings are used to determine the size of the PV array and the ESS, respectively. The higher the number of parallel strings, the more locally produced and stored power that can be used to charge the BEBs in the depot, but also the higher the investment cost for the PTO. The other variables are linked to the EMS and will optimize the daily operation of the depot microgrid.

2.3.1. Objective Function

The cost function that will be minimized by the PSO contains the capital costs (C_{CAPEX}), the replacement costs (C_{REP}), and the operational expenses (C_{OPEX}), as expressed in Equation (15).

$$C_{tot} = C_{CAPEX} + C_{REP} + C_{OPEX} \quad (15)$$

The capital costs include the investment costs for the different elements of the depot microgrid as given in Equation (16). The individual capital costs for each element are expressed in Equations (17)–(20).

$$C_{CAPEX} = \alpha \cdot (C_{C,PV,tot} + C_{C,ESS,tot} + C_{C,depot,tot} + C_{C,grid,tot}) \quad (16)$$

where α denotes a weight factor to include cooling, wiring, installation costs, taxes, etc.

$$C_{C,PV,tot} = P_{PV,mpptot} \cdot (C_{C,PV} + C_{C,DC/DC,PV}) \quad (17)$$

where $P_{PV,mpptot}$ denotes the maximum power that the PV array can produce [kWp] and $C_{C,PV}$ and $C_{C,DC/DC,PV}$ are the investment cost of the PV array and its DC/DC converter, respectively [€/kWp].

$$C_{C,ESS,tot} = E_{ESS,tot} \cdot (C_{C,ESS} + C_{C,DC/DC,ESS}) \quad (18)$$

where $E_{ESS,tot}$ is the total capacity of the ESS [kWh] and $C_{C,ESS}$ and $C_{C,DC/DC,ESS}$ are the investment cost of the ESS and its DC/DC converter, respectively [€/kWh].

$$C_{C,depot,tot} = P_{depot,tot} \cdot (C_{C,depot} + C_{C,DC/DC,depot}) \quad (19)$$

with $P_{depot,tot}$ the total power of the charging infrastructure [kW] and $C_{C,depot}$ and $C_{C,DC/DC,depot}$ the investment cost of the charging points and their DC/DC converters, respectively [€/kW].

$$C_{C,grid,tot} = S_{grid,tot} \cdot C_{C,transformer} + P_{grid,tot} \cdot C_{C,INV,grid} \quad (20)$$

where $S_{grid,tot}$ is the maximum apparent power of the grid connection [kVA] and $P_{grid,tot}$ is the maximum active power that the distribution grid can provide [kW]. Both parameters depend on the maximum total power of the charging infrastructure and the maximum power of the ESS. $C_{C,transformer}$ and $C_{C,INV,grid}$ denote the investment cost of the transformer [€/kVA] and the two-stage inverter [€/kW], respectively.

The replacement costs can be calculated in a similar way as the capital costs, considering the estimated investment cost of the components in the future and the number of replacements that will take place during the lifetime of the microgrid.

The operational costs comprise the maintenance costs and the electricity charges as expressed in Equations (21)–(24). The cost for consuming electricity from the grid is estimated by running a simulation model of the microgrid depot including the EMS and its

design variables. It covers an entire year to consider the effect of different environmental conditions and electricity prices.

$$C_{\text{OPEX}} = (1 + \beta)^{N_y} \cdot (C_{\text{M,tot}} + C_{\text{O,grid,tot}}) \quad (21)$$

where N_y denotes the lifetime of the microgrid [years] and β is a weight factor to consider the inflation rate of the electricity prices and the increasing maintenance costs over the lifetime of the depot microgrid.

$$C_{\text{M,tot}} = C_{\text{M,PV}} + C_{\text{M,bat}} + C_{\text{M,depot}} + C_{\text{M,transformer}} \quad (22)$$

$$C_{\text{M,x}} = N_y \cdot p_x \cdot C_{\text{C,x,tot}} \quad (23)$$

where p_x is a constant indicating the percentage of the investment cost that is considered for the maintenance cost of an element of the microgrid.

$$C_{\text{O,grid,tot}} = \sum_n P_{\text{grid}_n} \cdot \Delta t_n \cdot C_{\text{electricity}_n} \quad (24)$$

where P_{grid_n} is the power provided by or returned to the distribution grid during time slot n [kW], Δt_n is the length of time slot n [h], and $C_{\text{electricity}_n}$ is the electricity price [€/kWh].

An important constraint that should be included in the design optimization of the microgrid depot is the available area to install the PV array, as expressed in Equation (25). A similar constraint for the ESS is not considered because it has less strict space requirements.

$$A_{\text{PV,tot}} = A_{\text{PV}} \cdot N_{\text{s,PV}} \cdot N_{\text{p,PV}} \leq A_{\text{PV,tot,available}} \quad (25)$$

where $A_{\text{PV,tot}}$ denotes the total area of the PV array and A_{PV} the area of a single PV module.

2.3.2. Parameters

PSO is based on the social behavior of fish schools and bird flocks searching for food. A swarm of particles, each representing a candidate solution, moves through the search space with a certain velocity to find the optimal solution for the considered problem. At each iteration, a new position is reached by updating the velocity of the particles, as expressed in Equation (26). This happens according to the particle's best individual position from previous iterations ($x_{p,i}$), the best position of the entire swarm (x_g), and three control parameters, the inertia weight w , the cognitive acceleration coefficient c_1 , and the social acceleration coefficient c_2 .

$$\begin{aligned} v_i(t+1) &= w \cdot v_i(t) + c_1 \cdot r_1 \cdot (x_{p,i}(t) - x_i(t)) + c_2 \cdot r_2 \cdot (x_g(t) - x_i(t)) \\ x_i(t+1) &= x_i(t) + v_i(t+1) \end{aligned} \quad (26)$$

r_1 and r_2 are random variables between 0 and 1 to control the impact of the acceleration coefficients.

The control parameters significantly influence the performance of the PSO in terms of how close it can come to the best solution. The inertia weight affects the movement direction to keep the balance between exploitation and exploration. Typically, the inertia weight is first assigned with a high value to explore the entire search space. Across the iterations, it is gradually decreased to focus on the exploitation around the best solutions. The cognitive acceleration coefficient tends to move the particles towards their best individual positions, while the social acceleration coefficient affects the impact of the swarm to reach the best solution. A large difference between both acceleration coefficients will either cause the PSO to converge too fast towards an unacceptable solution or to not converge at all because the particles keep exploring.

Next to the control parameters, the swarm size is also vital for a good performance of the PSO as it characterizes its convergence. If the swarm size is too big, the computation time to find the best solution increases, while if the swarm is too small, it does not explore

the entire search space and can easily become trapped in suboptimal solutions. Table 1 presents the values of the control parameters and the population size applied in the co-design optimization of the depot microgrid. Stopping criteria are used to terminate the PSO when a predefined number of iterations is reached. Furthermore, for the initial swarm population, random values for all the variables are chosen within well-chosen minimum and maximum boundaries.

Table 1. Overview of the control parameters of the PSO.

Parameter	Value
Population size	$20 \times$ number of design variables
Inertia weight range	[0.1, 1.1]
Cognitive acceleration coefficient	1.49
Social acceleration coefficient	1.49
Stopping criteria (Total iterations)	30

3. Results and Discussions

3.1. Simulation Results

3.1.1. Use Case Description

The possible benefits of a depot microgrid are investigated for three different European cities. Brussels, Barcelona, and Gothenburg are selected because of their different environmental conditions and electricity tariffs, which can influence the results of the co-design optimization. These data are crucial to optimally design and manage the depot microgrid. For the solar irradiance and the temperature data of each city, hourly data records of 2021 from Solcast's database are used [31]. The hourly electricity prices are collected from the wholesale market websites for Belgium, Spain, and Sweden [32–34]. When electricity is bought from the distribution grid, an additional fixed cost of 0.15 €/kWh is applied to include network costs and charges. Electricity is sold to the grid at the wholesale market price.

The considered depot microgrid has 20 DC charging points, where each of them is connected to the DC link with DC/DC converters of 100 kW. When the DC/DC converters have a modular design, they consist of four modules of 25 kW. To allow a proper comparison of the use cases, the type of BEBs and their operation schedule is the same for the three cities. Standard 12 m buses with a battery capacity of 272 kWh and a nominal voltage of 600 V are considered [35]. Some BEBs will operate the entire day, while others will return back to the depot during the day to recharge before the evening rush hours. The arrival and departure times of the BEBs at the depot are detailed in Table 2. It is also assumed that they operate following the same planning every day. The daily charging schedules of the BEBs are provided by the HL CMS and its RTSO algorithm described in [20]. Preconditioning of the BEBs during cold mornings is considered as it has a substantial contribution to the power consumption of the depot. The considered lifetime of the depot, including charging points and DC/DC converters, is 25 years.

The depot microgrid has a DC link voltage of 750 V, which is a common and recommended voltage level for DC microgrids. Such high DC link voltages typically can be used for longer distances with reduced power line losses. Moreover, because 750 V is predominantly used for tram networks, PTOs may favor it for depot microgrids as well [36,37].

The total area that is available to install the PV array corresponds to the area above the 20 parking spots of the BEBs, as it can be mounted on a specific structure and on top of the workshop, where the BEBs are inspected and repaired. The PV array is modelled using the datasheet of a commercially available PV module (REC alpha series 380), which has an area of 2 m². Nine PV modules are connected in series to achieve a nominal voltage of 400 V. The number of parallel module strings and DC/DC converter modules is determined by the co-design optimization framework. The DC/DC converter modules each have a

power rating of 100 kW. The lifetime of the PV array and the converters is expected to be 25 years [38].

Table 2. Operation schedule of the BEBs for the considered cities.

BEB	Arrival Time Evening (h)	Departure Time Morning (h)	Arrival Time Day (h)	Departure Time Day (h)
BEB 1	18:15	5:50	-	-
BEB 2	18:25	6:20	-	-
BEB 3	18:30	6:15	-	-
BEB 4	18:35	6:15	-	-
BEB 5	18:40	6:40	-	-
BEB 6	18:45	6:30	-	-
BEB 7	18:50	6:45	-	-
BEB 8	19:10	6:50	-	-
BEB 9	19:15	7:00	-	-
BEB 10	20:30	7:40	-	-
BEB 11	21:00	8:30	-	-
BEB 12	22:15	4:30	10:45	14:20
BEB 13	22:30	4:55	11:10	14:50
BEB 14	22:40	5:30	12:00	15:10
BEB 15	22:45	5:20	12:15	15:30
BEB 16	23:00	5:35	12:30	15:55
BEB 17	23:15	6:00	13:10	16:30
BEB 18	23:20	5:45	13:25	16:00
BEB 19	23:40	6:05	13:30	17:00
BEB 20	0:10	6:10	14:15	18:10

The ESS is composed of batteries based on LFP technology, as this chemistry is particularly suited for storage system applications [39]. The number of parallel strings is again determined by the co-design optimization framework. Each parallel string consists of 125 battery cells with a capacity of 20 Ah, that are connected in series to reach a nominal voltage of 400 V. The SoC of the ESS is constrained between 20% and 90%. Typically, LFP batteries have an expected lifetime of 5000 full equivalent cycles, but for RES integration, 10,000 cycles are easily attainable if a charge and discharge rate of 0.5C is applied [40]. With 1–2 full cycles per day on average, the ESS can reach a lifetime of 13 years. The accompanying bidirectional DC/DC converter has modules of 100 kW each with an estimated lifetime of 18 years [38].

The grid inverter consists of modules with a power rating of 300 kW with an estimated lifespan of 20 years [41]. The transformer has modular units of 1000 kVA and a lifetime of 25 years. The total power rating of the grid is linked to the amount of charging points in the depot and the optimal size of the ESS.

An overview of all the technical specifications is provided in Table 3. The economic parameters of the depot microgrid, which are used for the TCO calculation, are presented in Table 4.

Table 3. Technical specifications of the depot microgrid.

Element	Parameter	Value
BEB	Battery voltage (V)	600
Microgrid	DC link voltage (V)	750
Microgrid	Number of charging points	20
Depot DC/DC	Power rating per module (kW)	100
Depot DC/DC	Lifetime (years)	25

Table 3. *Cont.*

Element	Parameter	Value
PV array	Open-circuit voltage (V)	400
PV array	Short-circuit current (A)	$N_{p,PV} \times 10.61$
PV array	Available area (m ²)	1800
PV array	Lifetime (years)	25
PV DC/DC	Power rating per module (kW)	100
PV DC/DC	Lifetime (years)	25
ESS	Nominal voltage (V)	400
ESS	Capacity (Ah)	$N_{p,bat} \times 20$
ESS	Lifetime (years)	13
ESS DC/DC	Power rating per module (kW)	100
ESS DC/DC	Lifetime (years)	20
Grid inverter	Power rating module (kW)	300
Grid inverter	Lifetime (years)	20
Transformer	Power rating unit (kVA)	1000
Transformer	Lifetime (years)	25

Table 4. Economic parameters of the depot microgrid [42–46].

Element	Parameter	Value
Microgrid	Weight factor CAPEX α	2.2
Microgrid	Weight factor OPEX β	0.01
Chargers	Investment cost (€/kW)	250
Chargers	Maintenance cost (% of CAPEX)	1
Depot DC/DC	Investment cost (€/kWp)	25
PV array	Investment cost (€/kWp)	300
PV array	Maintenance cost (% of CAPEX)	1
PV DC/DC	Investment cost (€/kWp)	25
ESS	Investment cost (€/kWh)	215
ESS	Replacement cost (future) (€/kWh)	93
ESS	Maintenance cost (% of CAPEX)	2
ESS DC/DC	Investment cost (€/kWh)	25
ESS DC/DC	Replacement cost (future) (€/kWh)	11
Grid inverter	Investment cost (€/kW)	70
Grid inverter	Replacement cost (future) (€/kWh)	35
Transformer	Investment cost (€/kVA)	15
Transformer	Maintenance cost (% of CAPEX)	1

3.1.2. Operation with Simple EMS

The results of the co-design optimization of the depot microgrid with the simple EMS for the three considered cities are detailed in Table 5. For each city, the PV array covers the entire available area to generate as much local power as possible. A depot microgrid in the city of Barcelona will have the largest ESS as it needs to store more excess solar power due to the more favorable environmental conditions. The ESSs for the depot microgrids in Brussels and Gothenburg have a similar size. The three cities also have a comparable maximum C-rate.

Table 5. Results of the co-design optimization for the considered cities utilizing the simple EMS.

City	$N_{p,PV}$	$N_{p,bat}$	$C_{r,ESS,max}$
Brussels	100	37	0.20
Barcelona	100	56	0.19
Gothenburg	100	37	0.23

The operation of the microgrid depots with the simple EMS is illustrated for a 72 h period in Figures 6–8, for Brussels, Barcelona, and Gothenburg, respectively: (a) shows the

electricity tariff, (b) presents the current that each subsystem supplies to or consumes from the microgrid, and (c) displays the SoC of the ESS. A positive current implies incoming current to the DC link of the microgrid; a negative current denotes outgoing current. For each use case, the SoC profile of the ESS shows a similar behavior as it is only charged with the excess power from the PV array. If the weather conditions allow it, this situation mainly occurs in the morning when the BEBs are driving around in the cities. From the moment that the BEBs return to the depot to recharge, the ESS will provide power to contribute to their charging demand until it is completely discharged. This often coincides with low-tariff periods, which is unfavorable in terms of operational costs. The maximum current at which charging and discharging can happen is defined by the optimized C-rate, which is also why the current profile of the ESS sometimes shows a constant value over a longer period of time. Furthermore, due to the high investment cost of the ESS, it is not possible to store all the locally produced energy on sunny days. The ESS is fully charged before the BEBs return to the depot and as a result, a part of the locally produced energy needs to be sent back to the distribution grid. Although the PTO receives money from the DSO for the excess microgrid energy generation, this energy will later need to be bought back at a higher price due to the additional network costs and the charges. From an operation point of view, it is thus clear that a better performance is feasible for all three use cases. This can be achieved using the advanced EMS.

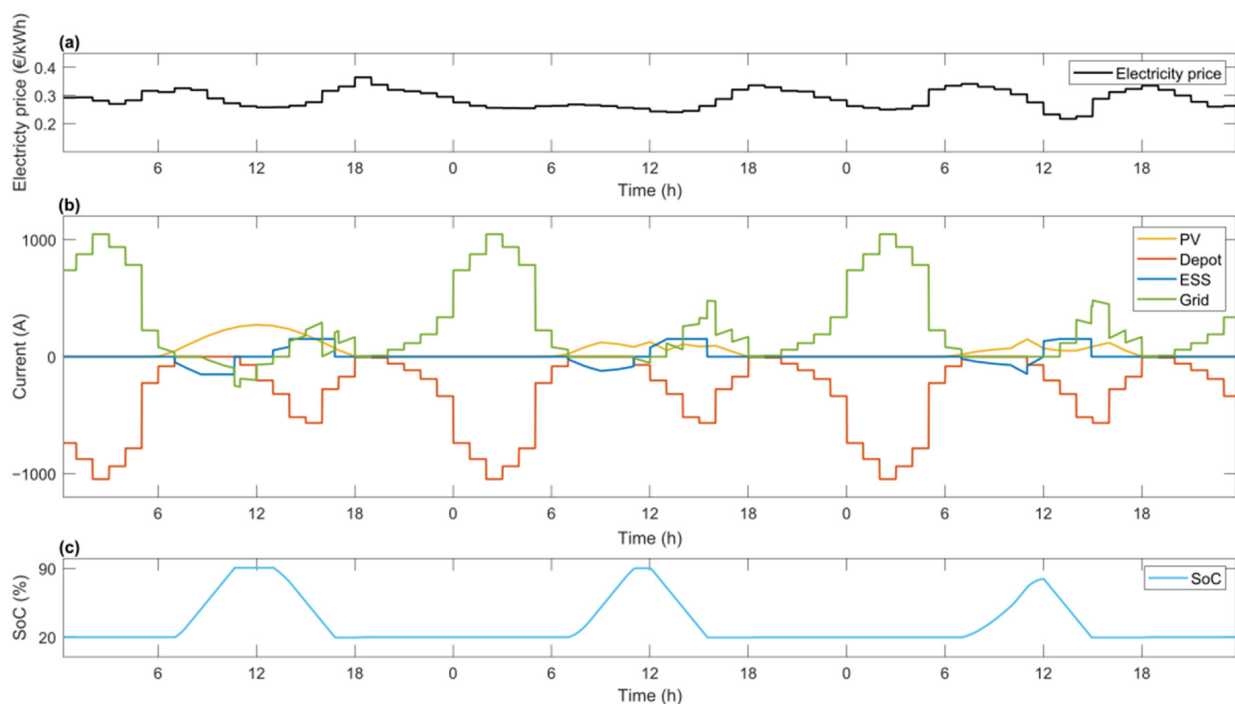


Figure 6. Simulation results illustrating the operation of the depot microgrid in Brussels with the simple EMS with (a) electricity tariff, (b) current of each subsystem, and (c) SoC of the ESS.

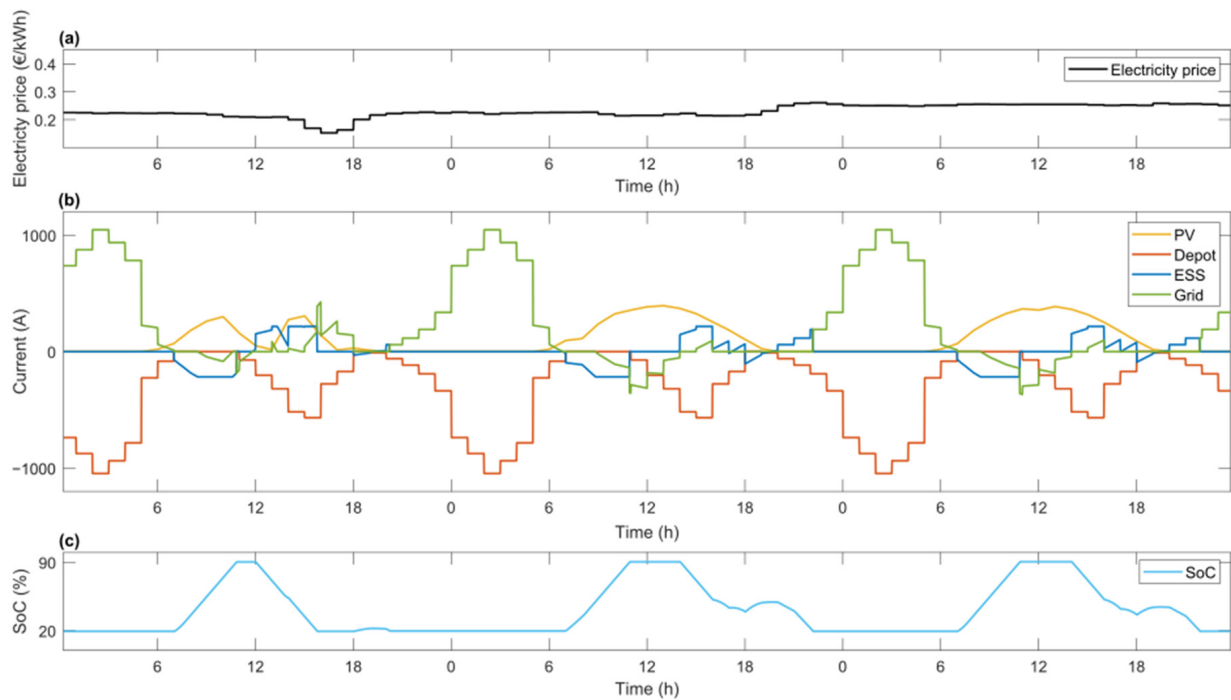


Figure 7. Simulation results illustrating the operation of the depot microgrid in Barcelona with the simple EMS with (a) electricity tariff, (b) current of each subsystem, and (c) SoC of the ESS.

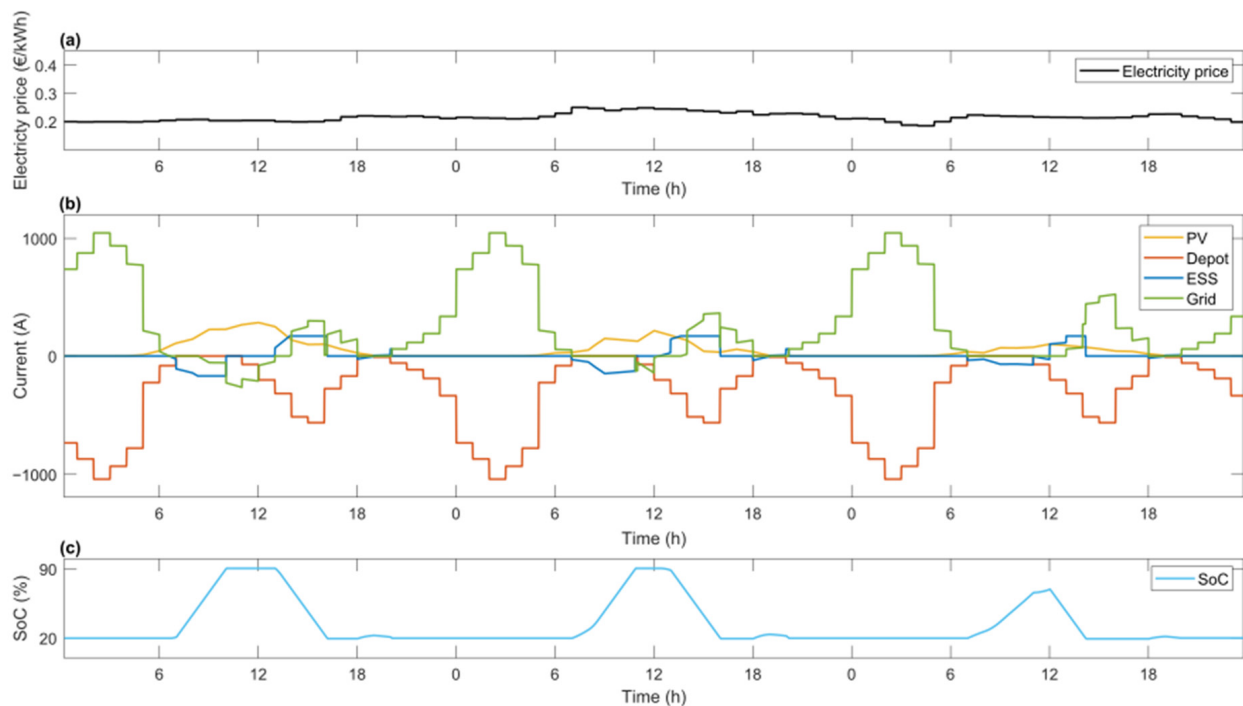


Figure 8. Simulation results illustrating the operation of the depot microgrid in Gothenburg with the simple EMS with (a) electricity tariff, (b) current of each subsystem, and (c) SoC of the ESS.

3.1.3. Operation with Advanced EMS

The results of the co-design optimization of the depot microgrid with the advanced EMS are presented in Table 6. In comparison with the optimal size of the ESS when using the simple EMS to operate the depot microgrid, the ESS is significantly larger with the advanced EMS. Accordingly, the investment cost for the PTO will also be higher. The ESS for the depot microgrid in Barcelona again has the largest size compared to its counterpart

in Brussels and Gothenburg. The maximum C-rates are almost identical for the three use cases. Their low values preserve the ESS from aging too quickly. For the design parameters of the advanced EMS, the main distinction between the use cases is the value of the constant A. For Brussels, a difference of 29% between the actual electricity price and the tariff in 4 h is a prerequisite to charge the ESS with power from the distribution grid. For Barcelona and Gothenburg, this is respectively 17% and 28%.

Table 6. Results of the co-design optimization for the considered cities utilizing the advanced EMS.

City	$N_{p,PV}$	$N_{p,bat}$	$C_{r,ESS,max}$	A	B	C	D
Brussels	100	67	0.13	1.29	0.63	0.62	0.55
Barcelona	100	97	0.15	1.17	0.68	0.63	0.38
Gothenburg	100	63	0.12	1.28	0.61	0.63	0.63

The operation of the microgrid depots in the three considered cities with the advanced EMS for the same 72 h period as the operation with the simple EMS is depicted in Figures 9–11. From the SoC profiles, it is clear that the ESS is much more used with the advanced EMS than with the simple EMS. The ESS is charged overnight if there is a noticeable difference between the low-tariff period at night and the high-tariff period in the morning. The ESS is then used in the morning to supply the charging demand of the BEBs. During the day, the ESS is charged with possible excess current from the PV infrastructure. Still, it can receive current from the grid before the high tariff period in the evening if the excess current of the PV system is not sufficient to fully charge the ESS or if a part of the stored energy is used to satisfy the charging demand during the day. As a result, the distribution grid is less used during the high-tariff periods and more during low-tariff periods, which decreases the operational costs for the PTO. Moreover, because the size of the ESS has increased, no or less excess power from the PV infrastructure needs to be sent back to the distribution grid in the morning, increasing the self-consumption of the depot microgrid.

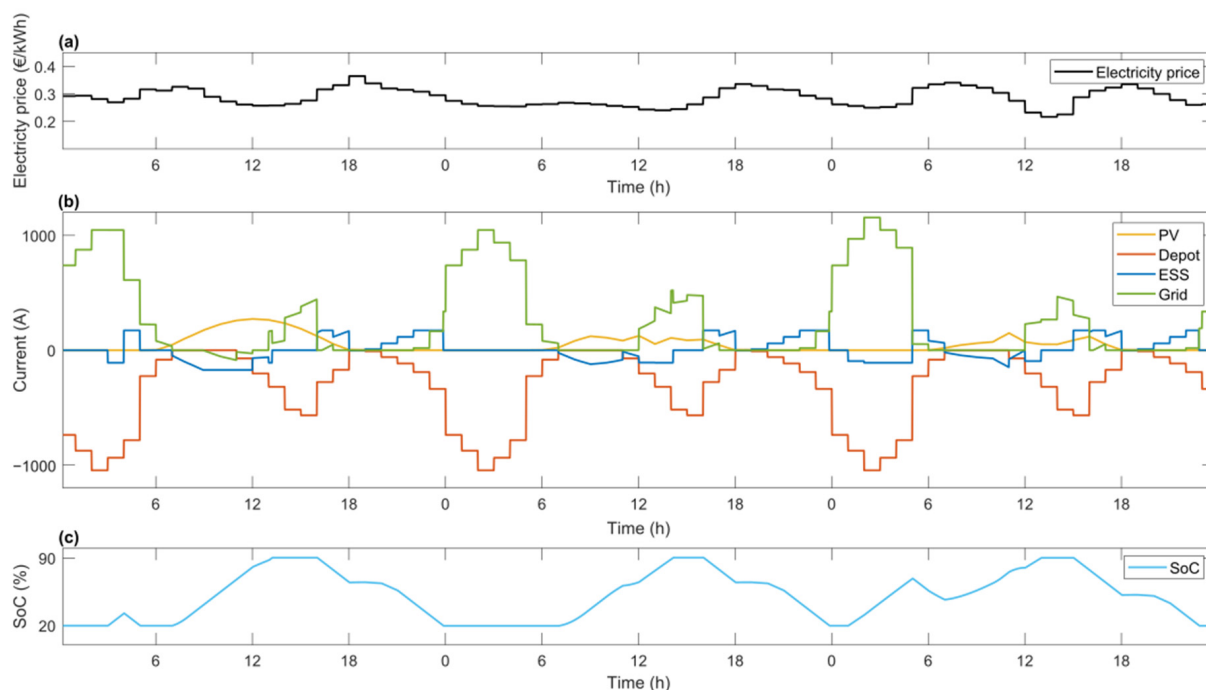


Figure 9. Simulation results illustrating the operation of the depot microgrid in Brussels with the advanced EMS with (a) electricity tariff, (b) current of each subsystem, and (c) SoC of the ESS.

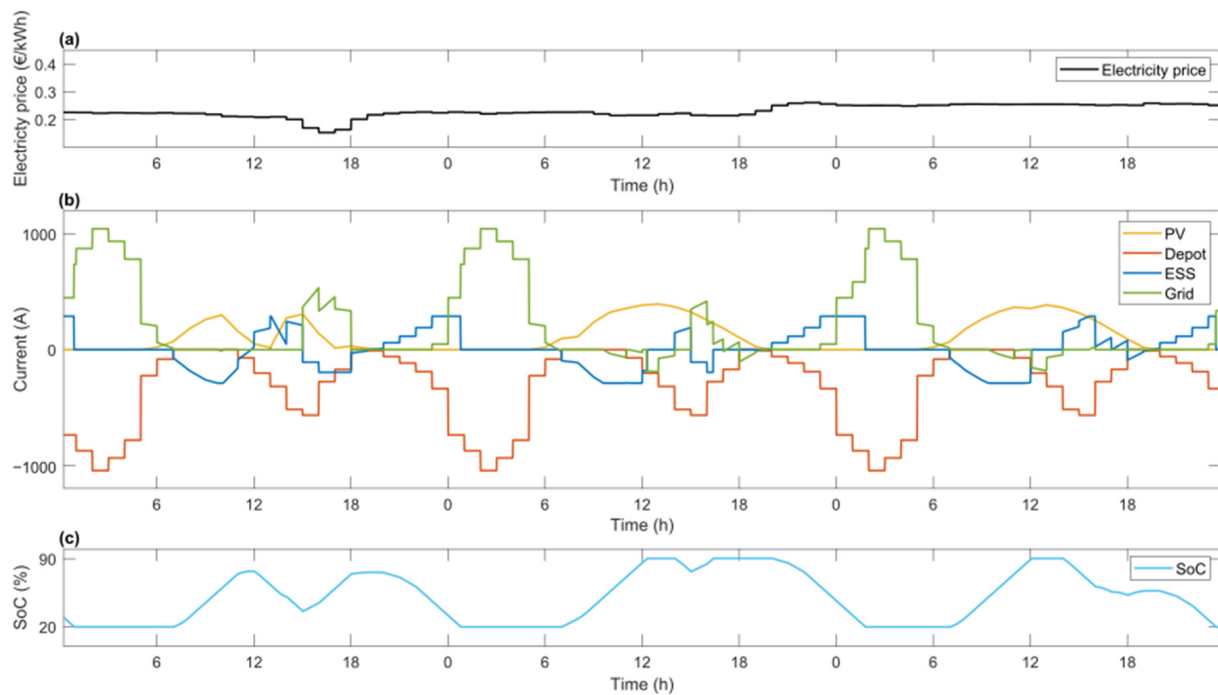


Figure 10. Simulation results illustrating the operation of the depot microgrid in Barcelona with the advanced EMS with (a) electricity tariff, (b) current of each subsystem, and (c) SoC of the ESS.

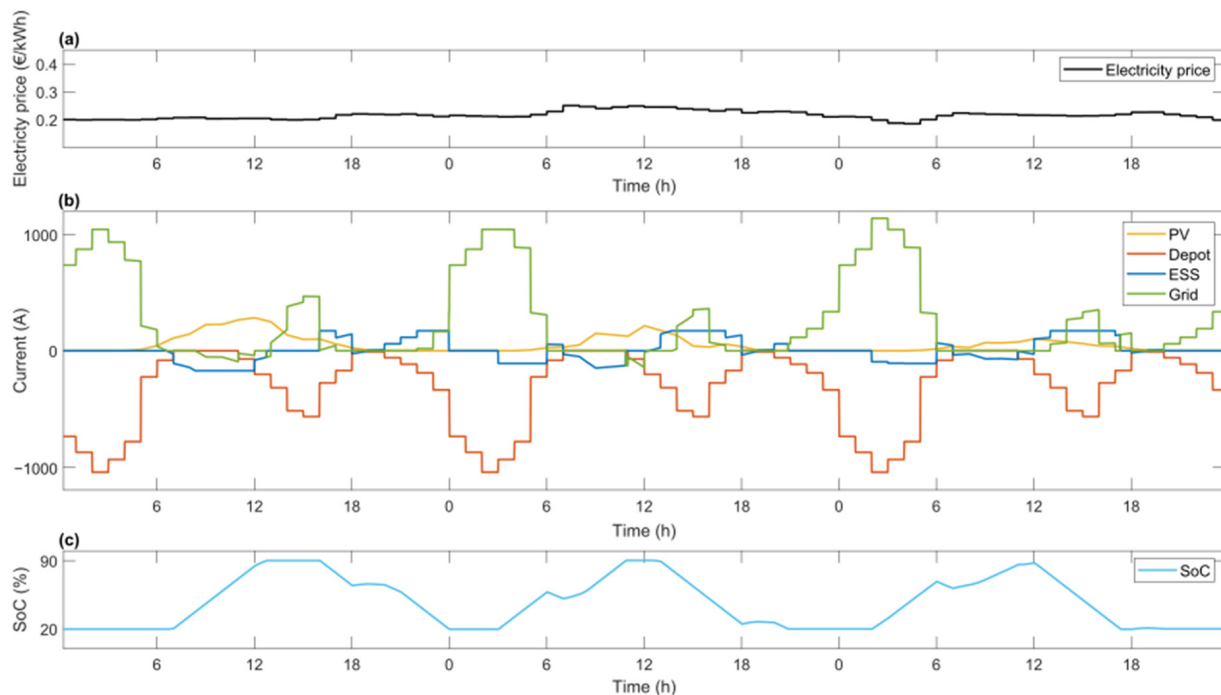


Figure 11. Simulation results illustrating the operation of the depot microgrid in Gothenburg with the advanced EMS with (a) electricity tariff, (b) current of each subsystem, and (c) SoC of the ESS.

3.1.4. TCO Analysis

A TCO comparison for the different locations of the depot microgrid is provided in Figure 12. It also shows the cost for different depot configuration scenarios. The baseline scenario, a standard depot which is only fed from the distribution grid and has no intelligent control strategies, is compared with a scenario where the depot is fitted with an HL-CMS,

and with the scenarios where a smart depot microgrid is additionally established with the simple and the more advanced EMS.

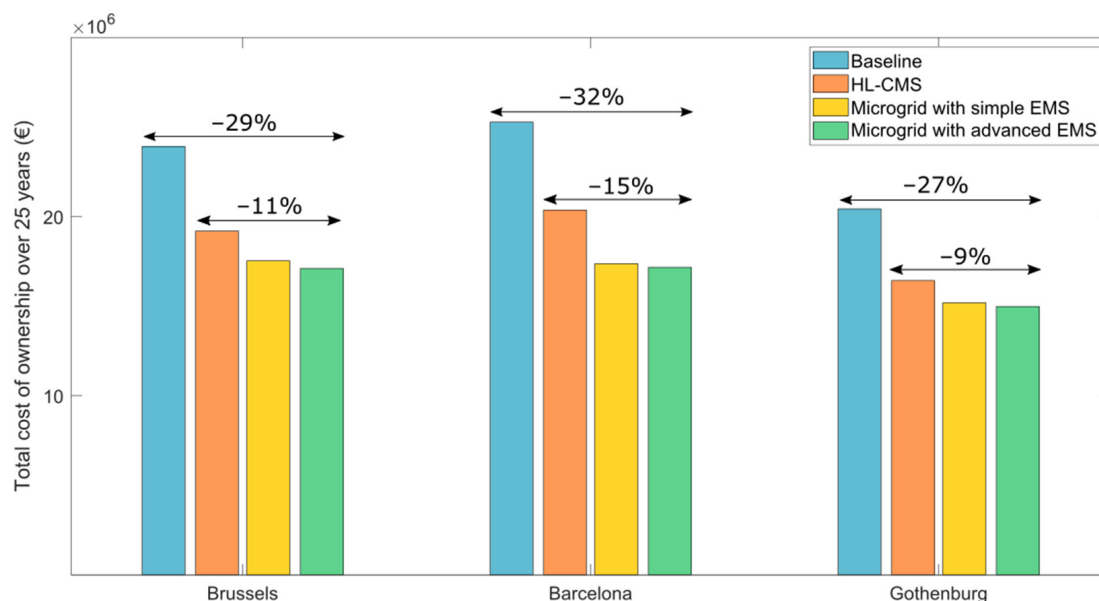


Figure 12. TCO comparison of different depot configurations in the considered cities.

It was already demonstrated in [20,47] that a smart charging algorithm could significantly reduce the operational and replacement costs for PTOs. For the considered depot where 20 BEBs can be charged, a TCO reduction of 20% over a period of 25 years can be achieved by using the HL-CMS and smart charging algorithm compared to a grid-only depot without any intelligent control strategies. However, by adding PV infrastructure and an ESS to construct a depot microgrid, the TCO is further reduced. For Brussels, an additional cost reduction of 11% is achieved over the entire lifetime of the microgrid compared with a depot that is only supervised by an HL-CMS. For Barcelona and Gothenburg, cost savings of respectively 15% and 9% are realized. In total, TCO reductions of around 30% compared to the baseline scenario are realistic.

The depot microgrid with an advanced EMS is the best option cost-wise, although the difference with a depot microgrid with a simple EMS is negligible (not more than 2%). The lower operational cost of the advanced EMS is practically eliminated by the higher investment cost. It can thus be concluded that the type of EMS is not the main parameter that affects the TCO, but rather the presence of the PV array and the ESS. A depot microgrid in the city of Gothenburg has the lowest TCO for all the scenarios, because the average annual electricity tariff is lower in Sweden than in Belgium and Spain. On the other hand, a depot microgrid in Barcelona will assure the highest cost savings compared with the baseline and the HL-CMS scenario since the more favorable, sunny conditions allow the PV infrastructure to generate more power that can be stored in the ESS. These results clearly show that environmental conditions and local electricity tariffs play an important role on the sizing and the performance of the depot microgrid.

The additional capital expenditures of the depot microgrid, regardless of which EMS is used, are compensated by the lower operational costs after 4–7 years, depending on the presence of an HL-CMS. This payback period is even tending to decrease with the expected decline of the total installed costs of PV infrastructure and ESSs.

3.2. Experimental Results

3.2.1. Hardware-in-the-Loop (HiL) Setup

As a depot microgrid typically consists of many different subsystems, acquiring all of them for HiL testing is not so simple because of the high investment costs. Therefore,

a simplified small-scale DC microgrid test setup is established in a lab environment to validate the proposed EMS.

The ESS is the most crucial component for maintaining the power balance within the microgrid. The EMS primarily controls the power flow from and towards the ESS. Accordingly, it should definitely be part of the small-scale DC microgrid. A battery pack consisting of four modules (3 kWh, 51.7 V, Eleo, Helmond, The Netherlands) connected in series serves as the ESS. A bidirectional DC/DC converter (40kW, 750V, Zekalabs, Sofia, Bulgaria), which connects the battery pack to the DC link of the microgrid, is also present as it receives the actual current reference from the EMS. The PV array and the accompanying unidirectional DC/DC converter are not available. As a consequence, a programmable DC test device (80 kW, 1000 V, Digatron, Aachen, Germany) acts as a PV emulator. A second, similar DC test device (80 kW, 1000 V, Digatron, Aachen, Germany) serves as the grid-tied inverter that normally connects the depot microgrid to the distribution grid. Both devices are, however, operated in a different way. The PV emulator is current-controlled and follows a predefined current profile that resembles the typical PV characteristic. The grid inverter emulator is voltage-controlled to maintain a constant DC link voltage, which is fixed at 400 V during the HiL tests. The different BEBs that are charged from the depot microgrid are represented by a single resistive load bank. Multiple resistors can be connected in series or parallel to increase or decrease the load of the DC microgrid test setup, resembling the arrival and departure of BEBs at a depot. A schematic overview of the power devices used in the microgrid is provided in Figure 13.

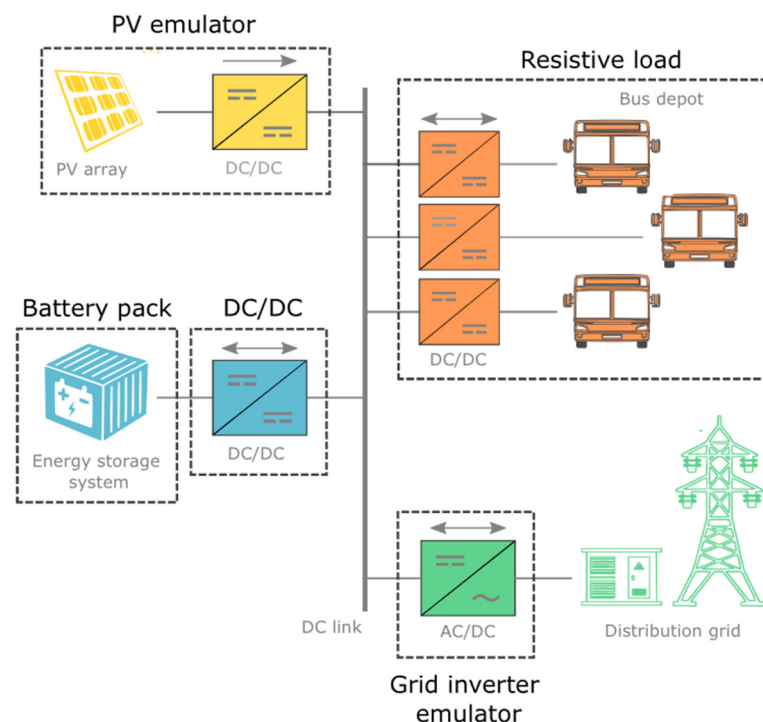


Figure 13. Overview of the power devices included in the HiL test setup to represent the depot microgrid.

To operate the bidirectional DC/DC converter in real time, the EMS is implemented in a control unit (dSpace Microlabbox, Paderborn, Germany) and sends the appropriate current setpoint to the converter via the CAN communication protocol. Because the EMS requires information about the SoC of the ESS, CAN communication is also established with the battery pack. Additionally, a number of DC current and voltage sensors are physically connected to the control unit as the EMS also needs measurements of the current originating from the PV emulator and the current flowing through the resistive load bank to maintain the energy balance within the microgrid. The voltage sensors, on the other

hand, are necessary to properly operate the DC/DC converter. Regardless of the operating mode, whether current must be sent from the battery to other components of the microgrid or vice-versa, it should always receive a setpoint for the output current. However, the EMS can only set the reference for the DC link side of the DC/DC converter, which is the input side when the battery pack needs to absorb energy from the microgrid. Accordingly, the reference of the EMS needs to be adjusted, which is performed based on the measurements of the battery pack voltage and the DC link voltage. Figure 14 depicts the complete HiL test setup of the small-scale DC microgrid, where each of the components are highlighted.

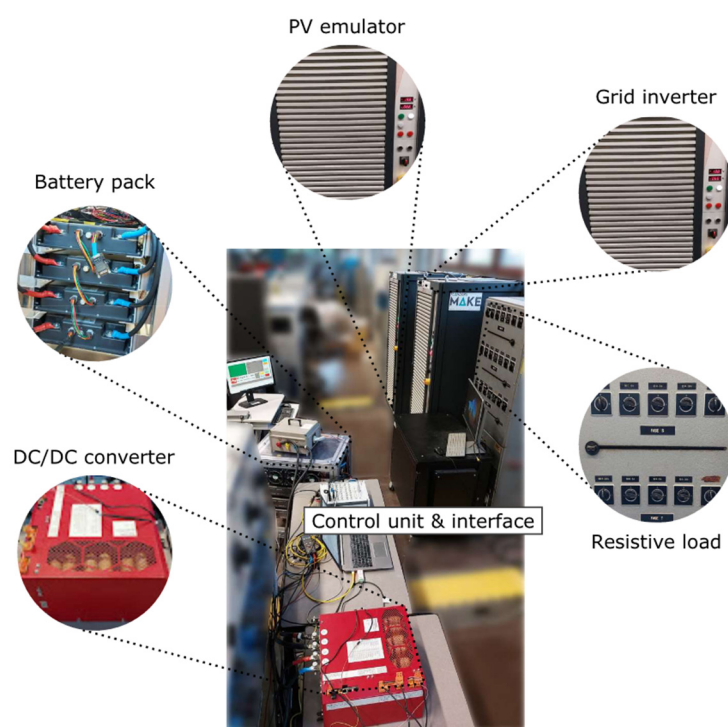


Figure 14. HiL test setup of a depot microgrid.

Only the advanced EMS is validated with the HiL tests because it covers more complex scenarios and reduces the operational costs more than the simple EMS. Since this EMS requires the electricity tariff forecasts as an input, they are included in the real-time model, which is executed in the control unit. For the design variables of the advanced EMS, optimal values from the use case of Brussels are used. A complete design optimization of the small-scale DC microgrid is not executed since the goal of the HiL tests is only to validate the EMS and maintaining the energy balance in real time. Nevertheless, because the resistive load can only consume a current of maximum 20 A, the current limit of other subsystems is scaled accordingly in order to reproduce a fairly realistic scenario during testing. To limit the testing time, the electricity tariff as well as the PV emulator current profile are updated every minute. The resistive load is manually changed on a regular basis in accordance with a typical depot charging profile.

3.2.2. Hardware-in-the-Loop (HiL) Test Results

The results of the experimental validation of the advanced EMS are shown in Figure 15, where (a) shows the electricity tariff and (b) presents the current that each subsystem supplies to or consumes from the microgrid. A positive current implies that current flows towards the DC link of the microgrid whereas a negative current indicates that current flows away from it.

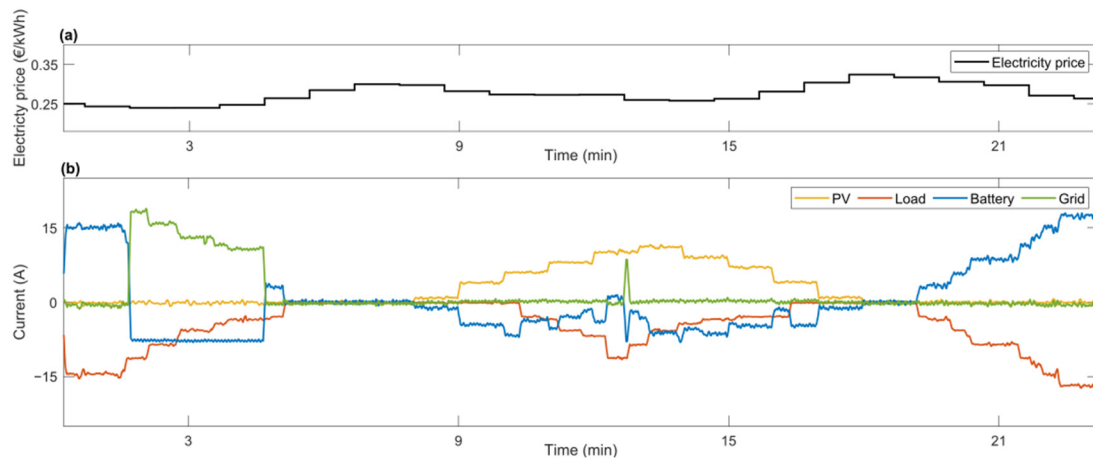


Figure 15. Experimental test results of the EMS for the DC microgrid with (a) electricity tariff and (b) current of each subsystem.

The results of the HiL test clearly show a robust behavior of the implemented EMS under different scenarios. At the beginning, the full charging load is covered by the battery pack. After a little less than 2 min, the grid takes over the supply of the load and even charges the battery pack because of the high difference between the electricity tariff at that point and the upcoming increased prices. This behavior was also noticed in the simulation results of the advanced EMS. After a period where there is no current exchange between the components of the microgrid, the PV emulator starts generating current. The battery pack stores the excess current, which is highly dynamic due to the resistive load that is operated at the same time, representing BEBs that return to the depot during the day. At the end, the battery again fully satisfies the load current on its own.

4. Conclusions

In this paper, an extensive analysis of a smart depot microgrid is presented. It consists of BEB charging infrastructure, a PV array, an ESS, a connection to the distribution grid, and the necessary PECs to connect the different subsystems. To control the power flow within the depot microgrid, a rule-based EMS is implemented. Two versions, a simple and a more advanced EMS, are developed to investigate how they influence the operation of the depot microgrid. The size of the subsystems of the microgrid and the values of the design variables of the EMSs are optimized using a co-design optimization framework, which aims to minimize the TCO of the depot microgrid over a lifetime of 25 years.

The simulation results of an entire year show that the more advanced EMS enables the usage of a larger ESS, which increases the self-consumption of the depot microgrid and decreases the operational costs. The latter is further decreased by charging the ESS during the low-tariff periods and discharging it during the high-tariff periods. However, after analyzing the TCO of a depot microgrid for three different cities with the simple and the advanced EMS, only a minor difference in favor of the advanced EMS was observed. Still, compared with a BEB depot without any intelligent control strategies and that is solely connected to the distribution grid, establishing a depot microgrid reduces the charging-related costs by up to 32%.

The experimental validation of the advanced EMS on a scaled-down HiL test setup revealed that it performs well in various operational scenarios of the microgrid. This is an important accomplishment as it will help to accelerate the incorporation EMS algorithms in real BEB depots in cities.

Future work could include adding additional elements, such as a light-rail network, to the depot microgrid. Several depot microgrids could also be interconnected to further reduce the operational costs for PTOs and lower the impact on the distribution grid. This increases the complexity of the system and requires more advanced, decentralized EMS

algorithms, based on data-driven machine learning techniques. A future EMS of a depot microgrid should also address health management of the ESS and the PECs, as well as protection and fault detection.

Author Contributions: Conceptualization, B.V.; methodology, B.V.; investigation, B.V.; software, B.V.; validation, B.V.; resources, T.G. and O.H.; data curation, O.H.; writing—original draft preparation, B.V.; writing—review and editing, B.V., T.G. and O.H.; visualization, B.V.; supervision, O.H.; project administration, T.G.; funding acquisition, O.H. All authors have read and agreed to the published version of the manuscript.

Funding: This research received no external funding.

Data Availability Statement: Data are contained within the article.

Acknowledgments: The authors acknowledge Flanders Make for their support to this research group.

Conflicts of Interest: The authors declare no conflicts of interest.

Abbreviations

BEB	battery electric bus
DSO	distribution system operator
EMS	energy management strategy
ESS	energy storage system
HiL	hardware-in-the-loop
HL-CMS	high-level charging management system
LuT	look-up table
MPPT	maximum power point tracking
OCV	open-circuit voltage
PEC	power electronic converter
PSO	particle swarm optimization
PTO	public transport operator
PV	photovoltaic
RES	renewable energy source
SoC	state-of-charge
TCO	total cost of ownership
V2G	vehicle-to-grid

References

- International Energy Agency (IEA). Global EV Outlook 2024 Moving Towards Increased Affordability. 2024. Available online: <https://www.iea.org/reports/global-ev-outlook-2024> (accessed on 21 October 2024).
- Dragičević, T.; Lu, X.; Vasquez, J.C.; Guerrero, J.M. DC Microgrids—Part I: A Review of Control Strategies and Stabilization Techniques. *IEEE Trans. Power Electron.* **2016**, *31*, 4876–4891. [CrossRef]
- Zia, M.F.; Elbouchikhi, E.; Benbouzid, M. Microgrids energy management systems: A critical review on methods, solutions, and prospects. *Appl. Energy* **2018**, *222*, 1033–1055. [CrossRef]
- Dougier, N.; Celik, B.; Chabi-Sika, S.-K.; Sechilariu, M.; Locment, F.; Emery, J. Modelling of Electric Bus Operation and Charging Process: Potential Contribution of Local Photovoltaic Production. *Appl. Sci.* **2023**, *13*, 4372. [CrossRef]
- Islam, S.M.M.; Salema, A.A.; Saleheen, M.Z.; Lim, J.M.Y. The influence of shifting the electric bus charging routine on the techno-economic performance of a solar-powered bus depot. *Energy* **2021**, *239*, 122316. [CrossRef]
- Arif, S.M.; Lie, T.T.; Seet, B.C.; Ayyadi, S. A novel and cost-efficient energy management system for plug-in electric bus charging depot owners. 2021, 199, 107413. *Electr. Power Syst. Res.* **2021**, *199*, 107413. [CrossRef]
- Zhuang, P.; Liang, H. Stochastic Energy Management of Electric Bus Charging Stations With Renewable Energy Integration and B2G Capabilities. *IEEE Trans. Sustain. Energy* **2020**, *12*, 1206–1216. [CrossRef]
- Liu, K.; Gao, H.; Liang, Z.; Zhao, M.; Li, C. Optimal charging strategy for large-scale electric buses considering resource constraints. *Transp. Res. Part D Transp. Environ.* **2021**, *99*, 103009. [CrossRef]
- Fan, H.; Wang, D.; Yu, Z.; Du, L. Bilevel Optimal Scheduling of Electric Bus Fleets in Regional Integrated Electricity–Gas–Heat Energy Systems. *IEEE Trans. Transp. Electr.* **2022**, *9*, 2792–2807. [CrossRef]
- Ren, H.; Ma, Z.; Fong, A.M.L.; Sun, Y. Optimal deployment of distributed rooftop photovoltaic systems and batteries for achieving net-zero energy of electric bus transportation in high-density cities. *Appl. Energy* **2022**, *319*, 119274. [CrossRef]

11. Al-Ismaïl, F.S. DC Microgrid Planning, Operation, and Control: A Comprehensive Review. *IEEE Access* **2021**, *9*, 36154–36172. [CrossRef]
12. Planas, E.; Andreu, J.; Gárate, J.I.; de Alegría, I.M.; Ibarra, E. AC and DC technology in microgrids: A review. *Renew. Sustain. Energy Rev.* **2015**, *43*, 726–749. [CrossRef]
13. Lotfi, H.; Khodaei, A. AC Versus DC Microgrid Planning. *IEEE Trans. Smart Grid* **2015**, *8*, 296–304. [CrossRef]
14. Vijay, A.S.; Doolla, S.; Chandorkar, M.C. Real-Time Testing Approaches for Microgrids. *IEEE J. Emerg. Sel. Top. Power Electron.* **2017**, *5*, 1356–1376. [CrossRef]
15. von Jouanne, A.; Agamloh, E.; Yokochi, A. Power Hardware-in-the-Loop (PHIL): A Review to Advance Smart Inverter-Based Grid-Edge Solutions. *Energies* **2023**, *16*, 916. [CrossRef]
16. Mahmud, R.; Jun, M.; Zhu, X.; Mishra, P.; Mohamed, A.A.; Meintz, A. Grid impact analysis using controller-hardware-in-the-loop for high-power vehicle charging stations. *Sustain. Energy Grids Netw.* **2022**, *32*, 100883. [CrossRef]
17. Meng, J.; Wang, Y.; Wang, C.; Wang, H. Design and implementation of hardware-in-the-loop simulation system for testing control and operation of DC microgrid with multiple distributed generation units. *IET Gener. Transm. Distrib.* **2017**, *11*, 3065–3072. [CrossRef]
18. Ferahtia, S.; Djeroui, A.; Rezk, H.; Houari, A.; Zeghlache, S.; Machmoum, M. Optimal control and implementation of energy management strategy for a DC microgrid. *Energy* **2021**, *238*, 121777. [CrossRef]
19. Wang, J.; Pratt, A.; Prabakar, K.; Miller, B.; Symko-Davies, M. Development of an integrated platform for hardware-in-the-loop evaluation of microgrids prior to site commissioning. *Appl. Energy* **2021**, *290*, 116755. [CrossRef]
20. Verbrugge, B.; Rauf, A.M.; Rasool, H.; Abdel-Monem, M.; Geury, T.; El Baghdadi, M.; Hegazy, O. Real-Time Charging Scheduling and Optimization of Electric Buses in a Depot. *Energies* **2022**, *15*, 5023. [CrossRef]
21. Karami, N.; Moubayed, N.; Outbib, R. General review and classification of different MPPT Techniques. *Renew. Sustain. Energy Rev.* **2017**, *68*, 1–18. [CrossRef]
22. Bollipo, R.B.; Mikkili, S.; Bonthagorla, P.K. Hybrid, optimization, intelligent and classical PV MPPT techniques: A Review. *CSEE J. Power Energy Syst.* **2021**, *7*, 9–33. [CrossRef]
23. Senturk, A.; Eke, R. A new method to simulate photovoltaic performance of crystalline silicon photovoltaic modules based on datasheet values. *Renew. Energy* **2017**, *103*, 58–69. [CrossRef]
24. Shuai, Z.; Fang, J.; Ning, F.; Shen, Z.J. Hierarchical structure and bus voltage control of DC microgrid. *Renew. Sustain. Energy Rev.* **2018**, *82*, 3670–3682. [CrossRef]
25. Gao, F.; Kang, R.; Cao, J.; Yang, T. Primary and secondary control in DC microgrids: A review. *J. Mod. Power Syst. Clean Energy* **2018**, *7*, 227–242. [CrossRef]
26. Han, Y.; Ning, X.; Yang, P.; Xu, L. Review of power sharing, voltage restoration and stabilization techniques in hierarchical controlled DC microgrids. *IEEE Access* **2019**, *7*, 149202–149223. [CrossRef]
27. Shami, T.M.; El-Saleh, A.A.; Alswaitti, M.; Al-Tashi, Q.; Summakieh, M.A.; Mirjalili, S. Particle Swarm Optimization: A Comprehensive Survey. *IEEE Access* **2022**, *10*, 10031–10061. [CrossRef]
28. Lorestani, A.; Gharehpetian, G.; Nazari, M.H. Optimal sizing and techno-economic analysis of energy- and cost-efficient standalone multi-carrier microgrid. *Energy* **2019**, *178*, 751–764. [CrossRef]
29. Phommixay, S.; Doumbia, M.L.; St-Pierre, D.L. Review on the cost optimization of microgrids via particle swarm optimization. *Int. J. Energy Environ. Eng.* **2019**, *11*, 73–89. [CrossRef]
30. Fioriti, D.; Poli, D.; Duenas-Martinez, P.; Micangeli, A. Multiple design options for sizing off-grid microgrids: A novel single-objective approach to support multi-criteria decision making. *Sustain. Energy Grids Netw.* **2022**, *30*, 100644. [CrossRef]
31. Solcast. Global Solar Irradiance Data and PV System Power Output Data. Available online: <https://solcast.com/> (accessed on 1 October 2022).
32. Elexys. Spot Belpex. Available online: <https://elexys.be/> (accessed on 1 April 2022).
33. OMI Polo Español S.A. (OMIE). Day-Ahead Market Hourly Prices in Spain. Available online: <https://www.omie.es/en> (accessed on 1 April 2022).
34. Nord Pool AS. Day-Ahead Prices. Available online: <https://www.nordpoolgroup.com/en> (accessed on 1 April 2022).
35. Bluebus. The Bluebus 12 m. Available online: <https://www.bluebus.fr/en/bluebus-12-m> (accessed on 24 June 2022).
36. Rodriguez-Diaz, E.; Chen, F.; Vasquez, J.C.; Guerrero, J.M.; Burgos, R.; Boroyevich, D. Voltage-Level Selection of Future Two-Level LVdc Distribution Grids: A Compromise Between Grid Compatibility, Safety, and Efficiency. *IEEE Electr. Mag.* **2016**, *4*, 20–28. [CrossRef]
37. Li, L.; Li, K.-J.; Sun, K.; Liu, Z.; Lee, W.-J. A Comparative Study on Voltage Level Standard for DC Residential Power Systems. *IEEE Trans. Ind. Appl.* **2022**, *58*, 1446–1455. [CrossRef]
38. Sandelic, M.; Sangwongwanich, A.; Blaabjerg, F. Impact of Power Converters and Battery Lifetime on Economic Profitability of Residential Photovoltaic Systems. *IEEE Open J. Ind. Appl.* **2022**, *3*, 224–236. [CrossRef]
39. Bajolle, H.; Lagadic, M.; Louvet, N. The future of lithium-ion batteries: Exploring expert conceptions, market trends, and price scenarios. *Energy Res. Soc. Sci.* **2022**, *93*, 102850. [CrossRef]
40. Olmos, J.; Gandiaga, I.; Saez-De-Ibarra, A.; Larrea, X.; Nieva, T.; Aizpuru, I. Modelling the cycling degradation of Li-ion batteries: Chemistry influenced stress factors. *J. Energy Storage* **2021**, *40*, 102765. [CrossRef]

41. Sangwongwanich, A.; Yang, Y.; Sera, D.; Blaabjerg, F. Mission Profile-Oriented Control for Reliability and Lifetime of Photovoltaic Inverters. *IEEE Trans. Ind. Appl.* **2019**, *56*, 601–610. [[CrossRef](#)]
42. Huber, J.E.; Kolar, J.W. Applicability of Solid-State Transformers in Today's and Future Distribution Grids. *IEEE Trans. Smart Grid* **2017**, *10*, 317–326. [[CrossRef](#)]
43. International Renewable Energy Agency. Electricity Storage and Renewables: Costs and Markets to 2030. 2017. Available online: https://www.connaissancedesenergies.org/sites/connaissancedesenergies.org/files/pdf-actualites/IRENA_Electricity_Storage_Costs_2017_Summary.pdf (accessed on 15 February 2023).
44. International Renewable Energy Agency. Renewable Power Generation Costs in 2021. 2022. Available online: <https://www.irena.org/Publications/2023/Aug/Renewable-Power-Generation-Costs-in-2022> (accessed on 15 February 2023).
45. Tsiropoulos, I.; Tarvydas, D.; Lebedeva, N. Li-ion batteries for mobility and stationary storage applications. In *Scenarios for Costs and Market Growth*; Publications Office of the European Union: Luxembourg, 2018. [[CrossRef](#)]
46. LaMonaca, S.; Ryan, L. The state of play in electric vehicle charging services—A review of infrastructure provision, players, and policies. *Renew. Sustain. Energy Rev.* **2021**, *154*, 111733. [[CrossRef](#)]
47. Verbrugge, B.; Rasool, H.; Hasan, M.M.; Chakraborty, S.; Geury, T.; El Baghdadi, M.; Hegazy, O. Reliability Assessment of SiC-Based Depot Charging Infrastructure with Smart and Bidirectional (V2X) Charging Strategies for Electric Buses. *Energies* **2022**, *16*, 153. [[CrossRef](#)]

Disclaimer/Publisher's Note: The statements, opinions and data contained in all publications are solely those of the individual author(s) and contributor(s) and not of MDPI and/or the editor(s). MDPI and/or the editor(s) disclaim responsibility for any injury to people or property resulting from any ideas, methods, instructions or products referred to in the content.